Supplementary Material for

Similarity of Scattering Rates in Metals Showing *T*-Linear Resistivity

J. A. N. Bruin, H. Sakai, R. S. Perry, A. P. Mackenzie

This PDF file includes:

a) Materials and methods

In order to study the low temperature resistivity of $Sr_3Ru_2O_7$ with high precision and accuracy, we prepared two needle-like single crystals (2 mm x 0.15 mm x 0.1 mm), each with residual resistivity less than 1 μΩcm. Each was mounted with *c*-axis aligned parallel to the applied magnetic field to within 1˚, in a bespoke cryostat in which cooling was controlled by the adiabatic demagnetisation of a salt pill mounted in a separate 6 T magnet. Standard low frequency (78 Hz) four-terminal techniques were employed, with transformers mounted at 1.8 K providing passive amplification of a factor of 100 and helping to achieve noise levels of < 50 pVHz$^{-1/2}$. Slow temperature sweeps (< 0.04 K / minute) were performed from 100 mK to 25 K at a set of fixed magnetic fields from 0 to 14 T. Temperature was measured using a calibrated Ge thermometer mounted in a zero field region. Careful comparison of warming and cooling runs ensured the acquisition of data for which the samples were in equilibrium with the thermometers at all temperatures. For a set of fields $0 < \mu_o H < 9$ T measurements to 400 K were also performed on the same samples using a commercial cryostat (Quantum Design PPMS).

b) Estimating the scattering rate from resistivity data

In this section we describe in detail how we estimate the scattering rates both for $Sr_3Ru_2O_7$ and the other materials for which data are shown in Fig. 2 of the paper. As stated in the text, we quote these rates per kelvin, as $\alpha k_B/\hbar$, with α a phenomenological dimensionless constant. We restricted our analyses to materials for which there is accurate data for Fermi volumes and velocities, mostly obtained from the de Haas-van Alphen effect. Many of the materials studied have multiple Fermi surface sheets. We describe the procedures for calculating the average scattering rate in such situations. Our analyses are in the isotropic scattering rate approximation *(16,17)*, and hence ignore potential sheet-to-sheet variations in the scattering rate, and variations of the Fermi velocity within individual sheets. These assumptions mean that the average errors in our quoted values of α are likely to be tens of percent in some cases. However, the similarities that we report across different material families are so surprising that errors of this order in α do not change the essence of our findings.

In each material we concentrate our analysis on the inelastic contribution to the scattering rate, subtracting out the residual resistivity due to elastic scattering. This residual term is typically small in the materials analysed, since they show de Haas-van Alphen oscillations. In $Sr_3Ru_2O_7$ the residual resistivity has some dependence on magnetic field and is approximately 2.5 μΩcm for the crystals studied here; increasing this by a factor of two by studying less pure crystals makes no qualitative difference to the inelastic scattering, providing empirical justification for the separation of the elastic and inelastic scattering terms.

Calculation of α for Sr₃Ru₂O₇

The 2D Fermi surface information proposed in Ref (*9*) is summarised in Table S1. The small deviations of the Fermi surface from perfect two-dimensionality would give corrections to α of only order 1%, so we work in a fully 2D approximation. Taking account of pocket multiplicities,

$$\alpha = \frac{\rho}{T}\frac{e^2}{2\pi k_\mathrm{B}d}\sum_i M_i\, k_{\mathrm{F}i} v_{\mathrm{F}i}$$

where ρ is the resistivity, d the bilayer-bilayer spacing of 10.35 Å, and M_i, $k_{\mathrm{F}i}$ and $v_{\mathrm{F}i}$ are the multiplicity, average Fermi wave vector and average Fermi velocity of Fermi surface pocket i.   Except for band #5 (γ_2), the effective masses are known to be almost independent of magnetic field, even though the specific heat coefficient C/T nearly doubles on the approach to H_c. There is no de Haas–van Alphen (dHvA) information on the field dependence of the mass of band #5, so either the field dependence of C/T is due to some non-quasiparticle excitations that have not yet been identified, or it is accounted for by a large change in the mass of the band #5 quasiparticles. The v_F values that we deduce in each of the two scenarios are shown in Table S1. The value that we calculate for α is insensitive to the choice of assumption, since in both cases band #5 has very small k_F and v_F.   The resistivity gradient is approximately 1.1 µΩcm / K, so α=1.5 (with velocity renormalisation for band #5) and 5% larger without velocity normalisation. In performing the calculation the Hall resistivity can safely be neglected, because it is only a few per cent of ρ (*45, 46*). For all temperatures considered in the paper, i.e. T < 400 K, $k_\mathrm{F}\ell \geq 1$ for almost all the quasiparticles in Sr₃Ru₂O₇, so our analysis is not sensitive to possible violations of the Mott-Ioffe-Regel limit which has been conjectured to apply to the high temperature resistivity of metals.

Table S1: List of Fermi surface information for Sr₃Ru₂O₇, deduced from the dHvA experiments (*9*). The carrier concentration n_i is calculated as $n_i = k_{\mathrm{F}i}^2/2\pi d$. For band #5, the Fermi velocity is estimated to be 0.84 x 10⁴ m/s from data from magnetocaloric oscillations. If we assume that the enhancement in specific heat coefficient as H approaches H_c arises from the mass renormalisation of this band, the velocity is renormalized to 0.26 x 10⁴ m/s at H=H_C.

Band	Type	F_i (kT)	Multiplicity M_i	$k_{\mathrm{F}i}$ (A⁻¹)	$v_{\mathrm{F}i}$ (10⁴m/s)	n_i (10²⁸m⁻³)
1 (α_1)	hole	1.78	1	0.23	3.9	0.083
2 (α_2)	hole	4.13	1	0.35	4.1	0.19
3 (β)	electron	0.15	2	0.07	1.4	0.014
4 (γ_1)	electron	0.91	4	0.17	2.5	0.17
5 (γ_2)	hole	0.11	8	0.06	0.84 (0T) → 0.26 (H_C)	0.041
6 (δ)	electron	0.43	2	0.11	1.6	0.040

Estimations of α from literature data

One of the striking features of Fig. 2 is that the materials for which it has been possible to estimate α vary in dimensionality from quasi 1D to fully 3D. Given this range, it is convenient to work with a generalised Drude expression. For a single Fermi surface pocket

$$\sigma = \frac{ne^2\tau}{m^*} = \frac{ne^2\tau v_F}{\hbar k_F}$$

in which $\hbar k_F/v_F$ for is given by the dHvA effective mass averaged across the pocket, k_F is the average Fermi wave vector of the pocket and the carrier concentration n is per m^3, taking into account the effective dimensionality:

$$n = \frac{2k_F}{\pi d_b d_c} \qquad \text{for one dimension,}$$

$$n = \frac{k_F^2}{2\pi d} \qquad \text{for two dimensions,}$$

$$n = \frac{k_F^3}{3\pi^2} \qquad \text{for three dimensions,}$$

where d_b and d_c are the distances between neighbouring conducting chains (along the a axis) in the direction of the b and c axes, respectively, while d is the distance between neighbouring conducting layers in a two-dimensional material.

For multiband materials, in the isotropic relaxation time approximation (*16, 17*), the expression becomes

$$\sigma = \tau \frac{e^2}{\hbar} \sum_i \frac{n_i v_{Fi}}{k_{Fi}}$$

and

$$\alpha = \frac{\hbar}{k_B \tau T} = \frac{e^2 \rho}{k_B T} \sum_i \frac{n_i v_{Fi}}{k_{Fi}}$$

in which n_i, v_{Fi} and k_{Fi} are the carrier concentration, average Fermi velocity and average Fermi wave vector associated with band i, and ρ is the total resistivity.

BaFe$_2$ (P$_{0.3}$ As$_{0.7}$)$_2$

Detailed dHvA measurements have been performed on one of the end-members of this solid solution, BaFe$_2$P$_2$ (*47*). They reveal two electron (α, β) and two hole (γ, δ) pockets, the Fermi surface information for which is summarised in Table S2. The behaviour of two electron pockets has been studied as a function of doping in two other papers (*25, 48*), showing that the overall carrier concentration decreases by about 35%. On the other hand, the renormalisation increases by a factor of 2.1 as the critical concentration is approached. The linear resistivity at the critical doping has $(\rho_{ab}-\rho_0)/T$ = 1.1 $\mu\Omega$cm / K (*24*), so assuming that the same trends apply to all the pockets, as discussed in ref. (*49*), α = 2.2.

Table S2: List of Fermi surface information for stoichiometric BaFe$_2$P$_2$, deduced from dHvA experiments (*47*). The dHvA frequencies for the α, β, and δ pockets are simply averaged among the extremal orbits, while that for the γ band that has a highly warped "dumbbell" surface around the top of the zone are obtained by averaging F$_{\gamma 1}$ and F$_{\gamma 2}$, weighting F$_{\gamma 1}$ by a factor of 2 [see Fig. 3 in Ref. (*47*)]. Assuming a quasi-two-dimensional Fermi surface, the carrier concentration n_i is calculated as $n_i = k_{Fi}^2/2\pi d$, where $d=c/2=6.2$ Å. The Fermi velocity for each pocket is calculated from the average effective mass. These quantities change as the critical concentration is approached, as described above.

Band	Type	F_i (kT)	Multiplicity M_i	k_{Fi} (A^{-1})	v_{Fi} (10^5m/s)	n_i (10^{28}m^{-3})
1 (α)	electron	1.3	1	0.20	1.4	0.10
2 (β)	electron	2.3	1	0.26	1.9	0.18
3 (γ)	hole	2.9	1	0.30	1.3	0.23
4 (δ)	hole	0.7	1	0.15	1.0	0.06

CeCoIn$_5$

The de Haas-van Alphen effect has been studied in detail in CeCoIn$_5$, for fields approaching the critical field of 5 T (parallel to [001]) from above. The Fermi surface is dominated by two sheets, each corresponding to approximately one carrier per formula unit. Based on the data of Refs. (*29, 30*), the sheet-averaged Fermi surface information is summarised in Table S3. Although the material is anisotropic, its resistive anisotropy is only about a factor of three for in-plane and out-of-plane transport. We therefore treat it as three-dimensional, and calculate the scattering rate based on the *T*-linear resistivity gradient averaged between in- and out-of-plane transport below 15 K (*28*). This gradient is 1.6 $\mu\Omega$cm / K, giving α = 1.0.

Table S3: Fermi surface information for the two main bands of CeCoIn$_5$, deduced from dHvA experiments (*29,30*). The average Fermi wave vector for each sheet is calculated by assuming a spherical Fermi surface: $k_{Fi} = (3\pi^2 n_i)^{\frac{1}{3}}$. The Fermi velocity for each sheet is calculated from the average effective mass. The effective mass for the hole band is significantly renormalised, and field-dependent. It is 83m_e at 9.3 T and extrapolated to be ~120m_e at the critical field (*29*). In the spin-resolved model in Ref. (*30*), the effective masses at 13-15 T for spin up and down are 46m_e and 154m_e, respectively, averaging to 100m_e. We here adopt m*~100m_e for the hole band as a typical value. Note that the value that we calculate for α is insensitive to the choice of the effective mass for the hole band, since

it is much heavier than that for the electron band that dominates the conductivity. The light electrons that dominate the conductivity are well-characterised by dHvA.

Band	Type	k_{Fi} (Å^{-1})	v_{Fi} (10^4 m/s)	n_i (10^{28} m^{-3})
1	electron	0.57	2.19	0.62
2	hole	0.57	0.66	0.62

CeRu$_2$Si$_2$

For this material, a metamagnetic transition is observed when a field is applied parallel to the c-axis (H_m=7.7 T). There are two dominant three-dimensional Fermi surfaces, a large hole sheet and a multiply-connected electron sheet. Based on LDA calculations (*50*), each has approximately 0.5 carriers per formula unit. The detailed Fermi surface information is summarised in Table S4, based on the dHvA experiments (*34, 51*). It has some anisotropy, but the transport anisotropy is small, justifying the use of a three-dimensional approximation. Considering the enhancement in specific heat [$\gamma(H=H_m)/\gamma(H=0$ T)=1.6] on the approach to the H_m (*52*), it is possible that the velocity for the heavy-mass hole sheet would be renormalized by approximately a factor of 1.6. The *T*-linear resistivity gradient is (ρ_{ab}-ρ_0)/*T* = 0.91 μΩcm / K for *H*=*H*$_m$ (*33*), so α = 1.1 without velocity renormalisation, and drops by only 4% if the extra velocity renormalisation is assumed.

We note that the resistivity of a fully two-dimensional metal with carrier concentration n_0 and Fermi velocity v_0 differs from that of a fully three-dimensional metal with the same values of n_0 and v_0 by only 30%. Materials like CeCoIn$_5$ and CeRu$_2$Si$_2$ sit between these two limits, so at the level of accuracy that we state for our estimations of α, the choice of effective dimension for the calculation is relatively unimportant.

Table S4: List of Fermi surface information for CeRu$_2$Si$_2$, deduced from LDA calculations (*50*) and dHvA experiments (*34, 51*). The average Fermi wave vector for each sheet is calculated by assuming a spherical surface with the same total carrier number. The average Fermi velocity for each sheet is calculated from the average effective mass. No extremal orbit has been observed for the large hole pocket for the field parallel to the c-axis, so we have here estimated velocity renormalisation from mass data for the field parallel to the a-axis for this pocket. However, we stress again that since the hole band is significantly renormalised ($m^* \sim 120 m_e$), the calculated value of α is insensitive to details of how the renormalisation is estimated. The light electrons that dominate the conductivity are well-characterised by dHvA.

Band	Type	k_{Fi} (Å^{-1})	v_{Fi} (10^4 m/s)	n_i (10^{28} m^{-3})
1	hole	0.56	0.54	0.58
2	electron	0.56	5.85	0.58

(TMTSF)$_2$PF$_6$

Although there is no conventional dHvA data for this quasi-1D charge transfer salt, a variety of experiments including cyclotron resonance measurements suggest an average carrier velocity of 2.0 x 10^5 ms^{-1} (27), approximately a factor of 1.3 lower than the free electron value for a 1D band with k_F = 0.2 Å^{-1} [1/4 filling, i.e., 0.5 carriers per molecule]. The carrier concentration is n = 1.36 x 10^{27} m^{-3} and the gradient of the linear resistivity at 11.8 kbar is 0.38 μΩcm / K (26), giving α = 0.9.

UPt$_3$

This material has a hexagonal structure, and shows a metamagnetic transition at around 20 T when a field is applied in the *a-b* plane. The temperature dependence of (ρ_c-ρ_0) at 20 T is proportional to *T* below 1 K. There, the resistivity gradient is (ρ_c-ρ_0)/*T* = 1.1 μΩcm / K (31). There are two dominant three-dimensional Fermi surfaces; a multiply-connected hole sheet and a large Γ-centred electron sheet. Average Fermi wave vectors and velocities are summarised in Table S5, based on dHvA experiments at fields of up to 18 tesla (32, 53). Specific heat data shows that [γ(*H*=20 T)/γ(*H*=18 T)=1.06] (54), so the possible velocity renormalisation on the approach to the critical field is of order only a few percent, which can be safely ignored here. Calculation based on the parameters of Table S5 then gives α = 1.1.

Table S5: List of Fermi surface information for UPt$_3$, deduced from dHvA experiments (32, 53). Each sheet appears to have 0.5-1 carriers per formula unit, so we here assume the carrier density is 0.75 carriers per formula unit for each as an average. The average Fermi wave vector for each sheet is calculated by assuming a spherical surface with the same total carrier number. The Fermi velocity for each pocket is calculated from the average effective mass at *H*=18 T .

Band	Type	k_{Fi} (Å^{-1})	v_{Fi} (10^4m/s)	n_i (10^{28}m^{-3})
1	hole	0.68	2.39	1.07
2	electron	0.68	0.88	1.07

Bi$_2$Sr$_2$Ca$_{0.92}$Y$_{0.08}$Cu$_2$O$_{8+\delta}$ (Bi2212) [Based on Ref. (21)]

The optical conductivity was fitted based on the Drude formula with a relaxation time of τ=A$\hbar$/(k_BT) (21). The best fitted results gives *A*=0.77, i.e., α=1.3 with the definition used in this paper. On the plot in Fig. 2, we use the Fermi velocity of 2.13 x 10^5 ms^{-1} deduced for this material from ARPES experiments (44) and the above value of α to fully determine the position of the point shown. The precise numerical value deduced for α in ref. (21) depended on an assumption for the value of the plasma frequency; by quoting that value here we implicitly accept that assumption.

Copper

The carrier density is $n = 8.5 \times 10^{28}$ m^{-3} and the quasiparticle mass is $m^*=1.3m_0$ (*55*). This gives v_F= 1.2 x 10^6 m/s and k_F=1.4 Å^{-1}. Based on analysis of a large number of experiments, Matula (*56*) has constructed a generic ρ-T for copper with a residual resistivity of 0.002 μΩcm. Extracting dρ/dT at 10K (for comparison with other data, acknowledging that at this temperature ρ is not T-linear) gives 1.2x10^{-5} μΩcm/K, resulting in α=1.7 x 10^{-3}. Between 100K and well above room temperature, ρ is approximately T-linear, with a gradient of 7.0 x 10^{-3} μΩcm/K (500-600 K). This results in α=1.0.

Gold

The carrier density is n=5.9 x 10^{28} m^{-3} and the quasiparticle mass is m^*=1.1m_0 (*55*). This gives v_F= 1.3 x 10^6 m/s and k_F=1.2 Å^{-1}. Based on analysis of a large number of experiments, Matula (*56*) has constructed a generic ρ-T for gold with a residual resistivity of 0.022 μΩcm. The gradient is essentially constant between 100K and well above room temperature, with a gradient of approximately 8.4 x 10^{-3} μΩcm/K, so α=0.96.

Silver

The carrier density is n=5.9 x 10^{28} m^{-3} and the quasiparticle mass is m^*=1.1m_0 (*55*). This gives v_F= 1.3 x 10^6 m/s and k_F=1.2 Å^{-1}. Based on analysis of a large number of experiments, Matula (*56*) has constructed a generic ρ-T for gold with a residual resistivity of 0.001 μΩcm. The gradient is essentially constant between 100 K and well above room temperature, with a gradient of approximately 6.1 x 10^{-3} μΩcm/K, so α=0.7.

Aluminium

From dHvA experiments (*57, 58*), there are two Fermi surfaces, consisting of a Γ-centred large hole sheet and a multiply-connected electron sheet. Sheet-averaged information is summarised in Table S6. At high temperatures at which ρ is T-linear its gradient is approximately 0.01 μΩcm/K (400-600 K) (*59*), so α = 1.1.

Table S6: Fermi surface information for aluminium, deduced from dHvA experiments (*57, 58*). The average Fermi wave vector for each sheet is calculated by assuming a spherical surface with the same total carrier number. The Fermi velocity for each sheet is calculated from the average effective mass.

Band	Type	k_{Fi} (Å^{-1})	v_{Fi} (10^5m/s)	n_i (10^{28}m^{-3})
1 (Γ−centred)	hole	1.22	10.6	6.1
2 (multiply−connected)	electron	0.26	3.6	0.06

Palladium

From dHvA experiments and electronic structure calculations (*60*), there are two Fermi surfaces consisting of a Γ-centred electron sheet and an open hole sheet. Sheet-averaged information is summarised in Table S7. The gradient of the high temperature resistivity is 0.03 $\mu\Omega$cm/K (400 K-500 K) (*56*), so α = 1.1.

Table S7: List of Fermi surface information for palladium, deduced from the dHvA experiments and KKR fitting (*60*). The average Fermi wave vector for each sheet is calculated by assuming a spherical surface with the same total carrier number. The Fermi velocity for each sheet is calculated from the average effective mass.

Band	Type	k_{Fi} (A^{-1})	v_{Fi} (10^5m/s)	n_i (10^{28}m^{-3})
1 (Γ-centred)	electron	0.91	5.5	2.5
2 (open)	hole	0.91	1.4	2.5

Niobium

From dHvA experiments and electronic structure calculations (*61, 62*), there are three Fermi surfaces consisting of a Γ-centred octahedral hole sheet, an open hole sheet, and N-centred ellipsoidal hole sheet. Sheet-averaged information is summarised in Table S8. The resistivity gradient is 0.049 $\mu\Omega$cm/K (250-300 K) (*63*), so α = 2.3.

Table S8: List of Fermi surface information for niobium, deduced from dHvA experiments and fitting to the results of electronic structure calculations (*61, 62*). The average Fermi wave vector for each sheet is calculated by assuming a spherical surface with the same total carrier number. The Fermi velocity for each sheet is calculated from the average effective mass.

Band	Type	k_{Fi} (A^{-1})	v_{Fi} (10^5m/s)	n_i (10^{28}m^{-3})
1 (octahedral)	hole	0.49	1.3	0.39
2 (open)	hole	0.95	3.1	2.9
3 (ellipsoidal)	hole	0.88	5.4	2.3

Lead

From dHvA experiments (*64*), there are two Fermi surfaces, consisting of a Γ-centred hole sheet and multiply-connected electron sheet. Sheet-averaged information is summarised in Table S9. The resistivity gradient is 0.071 $\mu\Omega$cm/K (around 300 K) (*65*), so α =2.7.

Table S9: Fermi surface information for lead, deduced from dHvA experiments (*64*). The average Fermi wave vector for each sheet is calculated by assuming a spherical surface with the same total carrier number.

Band	Type	k_{Fi} (A^{-1})	v_{Fi} (10^5m/s)	n_i (10^{28}m^{-3})
1 (Γ−centred)	hole	0.73	8.4	1.3
2 (multiply−connected)	electron	0.73	3.3	1.3

c) Parameters and error bars for Fig. 2 of main text

The key information from our study is encapsulated in the values of α whose estimation is described in section a) above. In order to plot all that information on a single graph, it is necessary to fix a convention for the parameters n, k_F and v_F that appear on the axes of Fig. 2 of the main text. The issue is how to calculate single parameters for each quantity for materials whose Fermi surfaces often contain more than one sheet.

For carrier concentration n, we adopted the convention that we would quote the total value, summed from the n_i of all the i Fermi surface sheets in each material. The Fermi wave vector k_F is defined depending on the effective dimension of each sheet by:

$$k_F = \sum_i k_{Fi} \quad \text{for one dimension,}$$

$$k_F^2 = \sum_i k_{Fi}^2 \quad \text{for two dimensions,}$$

$$k_F^3 = \sum_i k_{Fi}^3 \quad \text{for three dimensions,}$$

and is therefore approximately the Fermi wave vector that corresponds to the total carrier concentration.

For Fermi velocity we use a band-averaged number for easier comparison with average dHvA masses. We weight by (n_i/k_{Fi}), i.e. the average Fermi velocity is then calculated as:

$$v_F = \left(\sum_i v_{Fi} \right) \Big/ k_F \quad \text{for one dimension,}$$

$$v_F = \left(\sum_i k_{Fi} v_{Fi} \right) \Big/ k_F \quad \text{for two dimensions,}$$

$$v_F = \left(\sum_i k_{Fi}^2 v_{Fi} \right) \Big/ k_F \quad \text{for three dimensions,}$$

where, as above, $k_{\mathrm{F}}^{p} = \sum_i k_{\mathrm{F}i}^{p}$ (p=1, 2, and 3) for one-, two- and three-dimensional Fermi sheet, respectively.

These choices are fairly arbitrary, but alter only the appearance of Fig. 2. The calculated values for each material are summarized in Table S10.

The error bars for Fig. 2 are estimates based on a number of factors. For the y-axis, sources of error include experimental uncertainty in the measured resistivity, and uncertainty in estimating n and k_{F} for the materials with more complicated Fermi surfaces. For the x-axis, the uncertainty is in estimating band-averaged Fermi velocities from the mass data from the extremal dHvA orbits for which the mass has been measured, as well as in estimating n and k_{F}. Error values are listed for each material in Table S10. They are consistent with overall uncertainties of tens of per cent in α in the most unfavourable cases.

Table S10: Summary of the parameters used for the *x* and *y* axes of Fig. 2 of the main text, for all the materials shown in the figure. The definitions used are described above. An estimate of the *x* and *y* error bars for each material is also given. For $Bi_2Sr_2Ca_{0.92}Y_{0.08}Cu_2O_{8+\delta}$, the plotted point is based on an α value determined from optical conductivity and a literature value of v_F, and does not result from an analysis of resistivity data because of the large uncertainty about the Fermi surface of cuprates at optimal doping. We therefore do not include estimates of *n* and k_F for that material.

Material	n ($10^{28}m^{-3}$)	k_{Fi} (A^{-1})	v_{Fi} (10^5m/s)	x−axis error estimate (%)	y−axis error estimate (%)	α
$Sr_3Ru_2O_7$	0.54	0.59	0.78	15	15	1.5
$BaFe_2(As,P)_2$	0.37	0.38	1.1	30	25	2.1
$CeCoIn_5$	1.2	0.72	0.18	26	32	0.92
$(TMTSF)_2PF_6$	0.14	0.22	2.0	30	15	0.87
$CeRu_2Si_2$	1.2	0.70	0.40	23	20	1.1
UPt_3	2.1	0.86	0.21	27	28	1.1
Bi2212	−	−	2.1	10	−	1.3
Cu	8.5	1.36	12.1	0	5 (50% at 10 K)	1.0
Au	5.9	1.20	12.7	0	10	1.0
Ag	5.9	1.20	12.6	0	5	0.70
Al	6.2	1.22	10.7	7	8	1.1
Pd	5.1	1.14	4.0	12	8	1.1
Nb	5.6	1.18	5.3	4	7	2.3
Pb	2.6	0.92	7.4	26	30	2.8

d) Linear-scale plot of Fig. 2 from the main text
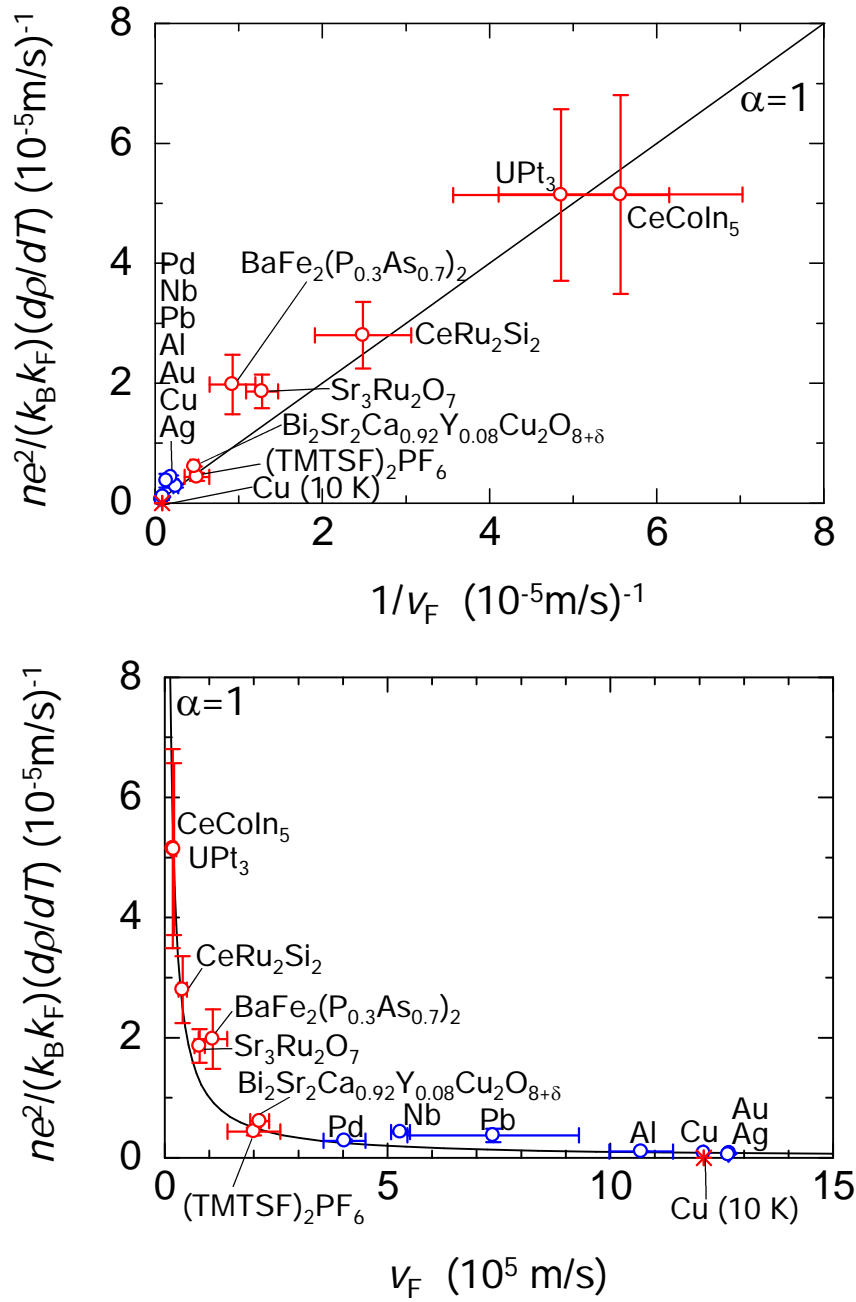
Fig. S1 Linear-scale plot of Fig. 2 from the main text. (Upper) As a function of $1/v_F$. (Lower) As a function of v_F. The black line marks $\alpha=1$.

e) Quantum critical metals with ρ ~ T^δ, $\delta \neq 1$

Throughout the paper, we have restricted our analysis and discussion to materials showing *T*-linear resistivity. However, other powers, notably $T^{1.5}$ and $T^{1.2}$, have also been widely observed in presumed quantum critical metals. Our main conclusion, namely that the origin of *T*-linear resistivity in correlated electron materials is scattering of quasiparticles from degrees of freedom associated with quantum criticality, suggests that different classes of scattering rather than completely different non-Fermi liquid states might eventually account for the different power laws that are observed. Further work would be required to clarify this issue.

References and Notes

1. G. R. Stewart, Non-Fermi-liquid behaviour in *d*- and *f*-electron metals. *Rev. Mod. Phys.* **73**, 797 (2001). doi:10.1103/RevModPhys.73.797

2. S. A. Grigera *et al.*, Magnetic field-tuned quantum criticality in the metallic ruthenate $Sr_3Ru_2O_7$. *Science* **294**, 329 (2001). doi:10.1126/science.1063539 Medline

3. R. S. Perry *et al.*, Multiple first-order metamagnetic transitions and quantum oscillations in ultrapure $Sr_3Ru_2O_7$. *Phys. Rev. Lett.* **92**, 166602 (2004). doi:10.1103/PhysRevLett.92.166602 Medline

4. S. A. Grigera *et al.*, Disorder-sensitive phase formation linked to metamagnetic quantum criticality. *Science* **306**, 1154 (2004). doi:10.1126/science.1104306 Medline

5. K. Kitagawa *et al.*, Metamagnetic quantum criticality revealed by ^{17}O-NMR in the itinerant metamagnet $Sr_3Ru_2O_7$. *Phys. Rev. Lett.* **95**, 127001 (2005). doi:10.1103/PhysRevLett.95.127001 Medline

6. P. Gegenwart, F. Weickert, M. Garst, R. S. Perry, Y. Maeno, Metamagnetic quantum criticality in $Sr_3Ru_2O_7$ studied by thermal expansion. *Phys. Rev. Lett.* **96**, 136402 (2006). doi:10.1103/PhysRevLett.96.136402 Medline

7. A. W. Rost, R. S. Perry, J. F. Mercure, A. P. Mackenzie, S. A. Grigera, Entropy landscape of phase formation associated with quantum criticality in $Sr_3Ru_2O_7$. *Science* **325**, 1360 (2009). doi:10.1126/science.1176627 Medline

8. A. W. Rost *et al.*, Thermodynamics of phase formation in the quantum critical metal $Sr_3Ru_2O_7$. *Proc. Natl. Acad. Sci. U.S.A.* **108**, 16549 (2011). doi:10.1073/pnas.1112775108 Medline

9. J. F. Mercure *et al.*, Quantum oscillations near the metamagnetic transition in $Sr_3Ru_2O_7$. *Phys. Rev. B* **81**, 235103 (2010). doi:10.1103/PhysRevB.81.235103

10. A. Tamai *et al.*, Fermi surface and van Hove singularities in the itinerant Metamagnet $Sr_3Ru_2O_7$. *Phys. Rev. Lett.* **101**, 026407 (2008). doi:10.1103/PhysRevLett.101.026407 Medline

11. Materials and methods are available as supplementary materials on *Science* Online.

12. L. Capogna *et al.*, Sensitivity to disorder of the metallic state in the ruthenates. *Phys. Rev. Lett.* **88**, 076602 (2002). doi:10.1103/PhysRevLett.88.076602 Medline

13. J. Zaanen, Superconductivity: Why the temperature is high. *Nature* **430**, 512 (2004). [doi:10.1038/430512a](doi:10.1038/430512a) Medline

14. R. A. Cooper *et al.*, Anomalous criticality in the electrical resistivity of $La_{2-x}Sr_xCuO_4$. *Science* **323**, 603 (2009). doi:10.1126/science.1165015 Medline

15. T. Schäfer, D. Teaney, Nearly perfect fluidity: From cold atomic gases to hot quark gluon plasmas. *Rep. Prog. Phys.* **72**, 126001 (2009). [doi:10.1088/0034-4885/72/12/126001](doi:10.1088/0034-4885/72/12/126001)

16. N. P. Ong, Geometric interpretation of the weak-field Hall conductivity in two-dimensional metals with arbitrary Fermi surface. *Phys. Rev. B* **43**, 193 (1991). doi:10.1103/PhysRevB.43.193 Medline

17. P. L. Taylor, The relaxation time of conduction electrons in the noble metals. *Proc. R. Soc. Lond. A Math. Phys. Sci.* **275**, 209 (1963). doi:10.1098/rspa.1963.0165

18. J. W. Orenstein *et al.*, Frequency- and temperature-dependent conductivity in $YBa_2Cu_3O_{6+x}$ crystals. *Phys. Rev. B* **42**, 6342 (1990). doi:10.1103/PhysRevB.42.6342 Medline

19. Z. Schlesinger *et al.*, Infrared studies of the superconducting energy gap and normal-state dynamics of the high-T_c superconductor $YBa_2Cu_3O_7$. *Phys. Rev. B* **41**, 11237 (1990). doi:10.1103/PhysRevB.41.11237 Medline

20. H. L. Liu *et al.*, Doping-induced change of optical properties in underdoped cuprate superconductors. *J. Phys. Condens. Matter* **11**, 239 (1999). [doi:10.1088/0953-8984/11/1/020](doi:10.1088/0953-8984/11/1/020)

21. D. van der Marel *et al.*, Quantum critical behaviour in a high-T_c superconductor. *Nature* **425**, 271 (2003). doi:10.1038/nature01978 Medline

22. C. C. Homes *et al.*, A universal scaling relation in high-temperature superconductors. *Nature* **430**, 539 (2004). doi:10.1038/nature02673 Medline

23. T. Valla *et al.*, Evidence for quantum critical behavior in the optimally doped cuprate $Bi_2Sr_2CaCu_2O_{8+\delta}$. *Science* **285**, 2110 (1999). doi:10.1126/science.285.5436.2110 Medline

24. S. Kasahara *et al.*, Evolution from non-Fermi- to Fermi-liquid transport via isovalent doping in $BaFe2_{As1−xPx}2$ superconductors. *Phys. Rev. B* **81**, 184519 (2010). doi:10.1103/PhysRevB.81.184519

25. H. Shishido *et al.*, Evolution of the Fermi surface of $BaFe2_{As1-xPx}2$ on entering the superconducting dome. *Phys. Rev. Lett.* **104**, 057008 (2010). doi:10.1103/PhysRevLett.104.057008 Medline

26. N. Doiron-Leyraud *et al.*, Linear-T scattering and pairing from antiferromagnetic fluctuations in the $(TMTSF)_2X$ organic superconductors. *Eur. Phys. J. B* **78**, 23 (2010). doi:10.1140/epjb/e2010-10571-4

27. J. S. Brooks, Magnetic field dependent and induced ground states in organic conductors. *Rep. Prog. Phys.* **71**, 126501 (2008). [doi:10.1088/0034-4885/71/12/126501](doi:10.1088/0034-4885/71/12/126501)

28. M. A. Tanatar, J. Paglione, C. Petrovic, L. Taillefer, Anisotropic violation of the Wiedemann-Franz law at a quantum critical point. *Science* **316**, 1320 (2007). doi:10.1126/science.1140762 Medline

29. R. Settai *et al.*, Quasi-two-dimensional Fermi surfaces and the de Haas–van Alphen oscillation in both the normal and superconducting mixed states of $CeCoIn_5$. *J. Phys. Condens. Matter* **13**, L627 (2001). [doi:10.1088/0953-8984/13/27/103](doi:10.1088/0953-8984/13/27/103)

30. A. McCollam, S. R. Julian, P. M. C. Rourke, D. Aoki, J. Flouquet, Anomalous de Haas-van Alphen oscillations in $CeCoIn_5$. *Phys. Rev. Lett.* **94**, 186401 (2005). doi:10.1103/PhysRevLett.94.186401 Medline

31. J. S. Kim, D. Hall, K. Heuser, G. R. Stewart, Indications of non-Fermi liquid behaviour at the metamagnetic transition of UPt_3. *Solid State Commun.* **114**, 413 (2000). [doi:10.1016/S0038-1098(00)00084-3](doi:10.1016/S0038-1098(00)00084-3)

32. N. Kimura *et al*., Fermi surface property of UPt_3 studied by de Haas-van Alphen and magnetoresistance experiments. *Physica B* **281-282**, 710 (2000). [doi:10.1016/S0921-4526(99)01229-6](doi:10.1016/S0921-4526(99)01229-6)

33. R. Daou, C. Bergemann, S. R. Julian, Continuous evolution of the Fermi surface of $CeRu_2Si_2$ across the metamagnetic transition. *Phys. Rev. Lett.* **96**, 026401 (2006). doi:10.1103/PhysRevLett.96.026401 Medline

34. M. Takashita *et al*., dHvA effect study of metamagnetic trasition in $CeRu_2Si_2$ II -The state above the metamagnetic transition. *J. Phys. Soc. Jpn.* **65**, 515 (1996). doi:10.1143/JPSJ.65.515

35. R. Hlubina, T. M. Rice, Resistivity as a function of temperature for models with hot spots on the Fermi surface. *Phys. Rev. B* **51**, 9253 (1995). doi:10.1103/PhysRevB.51.9253 Medline

36. A. Rosch, Interplay of disorder and spin fluctuations in the resistivity near a quantum critical point. *Phys. Rev. Lett.* **82**, 4280 (1999). doi:10.1103/PhysRevLett.82.4280

37. J. M. Ziman, *Electrons and Phonons* (Claredon Press, Oxford, 1960).

38. S. S. Adler *et al*., PHENIX Collaboration, Elliptic flow of identified hadrons in Au+Au collisions at sqrt sNN =200 GeV. *Phys. Rev. Lett.* **91**, 182301 (2003). doi:10.1103/PhysRevLett.91.182301 Medline

39. T. Schäfer, The shear viscosity to entropy density ratio of trapped Fermions in the unitarity limit. *Phys. Rev. A* **76**, 063618 (2007). doi:10.1103/PhysRevA.76.063618

40. C. Cao *et al*., Universal quantum viscosity in a unitary Fermi gas. *Science* **331**, 58 (2011). doi:10.1126/science.1195219 Medline

41. D. A. Teaney, Viscous hydrodynamics and the Quark-Gluon plasma, *arXiv*:0905.2433v1.

42. P. K. Kovtun, D. T. Son, A. O. Starinets, Viscosity in strongly interacting quantum field theories from black hole physics. *Phys. Rev. Lett.* **94**, 111601 (2005). doi:10.1103/PhysRevLett.94.111601 Medline

43. A. V. Andreev, S. A. Kivelson, B. Spivak, Hydrodynamic description of transport in strongly correlated electron systems. *Phys. Rev. Lett.* **106**, 256804 (2011). doi:10.1103/PhysRevLett.106.256804 Medline

44. A. Kaminski *et al*., Momentum anisotropy of the scattering rate in cuprate superconductors. *Phys. Rev. B* **71**, 014517 (2005). doi:10.1103/PhysRevB.71.014517

45. R. A. Borzi *et al*., Hall coefficient anomaly in the low-temperature high-field phase of Sr3Ru2O7. *Phys. Rev. B* **84**, 205112 (2011). doi:10.1103/PhysRevB.84.205112

46. R. S. Perry *et al*., Hall effect of $Sr_3Ru_2O_7$. *Physica B* **284-288**, 1469 (2000). [doi:10.1016/S0921-4526(99)02712-X](doi:10.1016/S0921-4526(99)02712-X)

47. B. J. Arnold *et al*., Nesting of electron and hole Fermi surfaces in nonsuperconducting $BaFe_2P_2$. *Phys. Rev. B* **83**, 220504 (2011). doi:10.1103/PhysRevB.83.220504

48. J. G. Analytis, J.-H. Chu, R. D. McDonald, S. C. Riggs, I. R. Fisher, Enhanced Fermi-surface nesting in superconducting BaFe2(As(1-x)P(x))2 revealed by the de Haas-van Alphen effect. *Phys. Rev. Lett.* **105**, 207004 (2010). doi:10.1103/PhysRevLett.105.207004 Medline

49. A. Carrington, Quantum oscillation studies of the Fermi surface of iron-pnictide superconductors. *Rep. Prog. Phys.* **74**, 124507 (2011). doi:10.1088/0034-4885/74/12/124507

50. H. Yamagami, A. Hasegawa, Local-density band theory for the Fermi surface of the heavy-electron compound CeRu2Si2. *J. Phys. Soc. Jpn.* **62**, 592 (1993). doi:10.1143/JPSJ.62.592

51. H. Aoki, S. Uji, A. K. Albessard, Y. Onuki, Transition of *f* electron nature from itinerant to localized: Metamagnetic transition in CeRu2Si2 studied via the de Haas-van Alphen effect. *Phys. Rev. Lett.* **71**, 2110 (1993). doi:10.1103/PhysRevLett.71.2110 Medline

52. J. Flouquet, P. Haen, S. Raymonda, D. Aoki, G. Knebel, Itinerant metamagnetism of CeRu2Si2: bringing out the dead. Comparison with the new Sr3Ru2O7 case. *Physica B* **319**, 251 (2002). doi:10.1016/S0921-4526(02)01126-2

53. G. J. McMullan *et al.*, The Fermi surface and *f*-valence electron count of UPt3. *New J. Phys.* **10**, 053029 (2008). doi:10.1088/1367-2630/10/5/053029

54. Z. Tarnawski *et al.* van Kempen H, Specific heat of UPt3 in magnetic fields up to 24.5 T. *Phys. Rev. B* **41**, 9352 (1990). doi:10.1103/PhysRevB.41.9352 Medline

55. N. W. Ashcroft, N. D. Mermin, *Solid State Physics* (HRW International Editions, Philadelphia, 1976).

56. R. A. Matula, Electrical-resistivity of copper, gold, palladium, and silver. *J. Phys. Chem. Ref. Data* **8**, 1147 (1979). doi:10.1063/1.555614

57. E. M. Gunnersen, The de Haas-van Alphen effect in aluminium. *Philos. Trans. R. Soc. Lond. A* **249**, 299 (1957). doi:10.1098/rsta.1957.0001

58. J. R. Anderson, S. S. Lane, High-frequency dc Haas-van Alphen oscillations in aluminum. *Phys. Rev. B* **2**, 298 (1970). doi:10.1103/PhysRevB.2.298

59. D. R. Lide, *CRC Handbook Chemistry and Physics* (CRC Press, New York, 1994).

60. D. H. Dye *et al.*, Fermi surface and many-body enhancement in Pd. *Phys. Rev. B* **23**, 462 (1981). doi:10.1103/PhysRevB.23.462

61. D. P. Karim, J. B. Ketterson, G. W. Crabtree, A de Haas-van Alphen study of niobium: Fermi surface, cyclotron effective masses, and magnetic breakdown effects. *J. Low Temp. Phys.* **30**, 389 (1978). doi:10.1007/BF00114959

62. G. W. Crabtree, D. H. Dye, D. P. Karim, S. A. Campbell, J. B. Ketterson, Anisotropy of the Fermi surface, Fermi velocity, many-body enhancement, and superconducting energy gap in Nb. *Phys. Rev. B* **35**, 1728 (1987). doi:10.1103/PhysRevB.35.1728 Medline

63. P. B. Allen *et al.*, dc transport in metals. *Phys. Rev. B* **34**, 4331 (1986). doi:10.1103/PhysRevB.34.4331 Medline

64. A. V. Gold, An experimental determination of the Fermi surface in lead. *Philos. Trans. R. Soc. Lond. A* **251**, 85 (1958). doi:10.1098/rsta.1958.0010

65. W. B. Pietenpol, H. A. Miley, Electrical resistivities and temperature coefficients of lead, tin, zinc, and bismuth in the solid and liquid states. *Phys. Rev.* **34**, 1588 (1929). doi:10.1103/PhysRev.34.1588